Structural Element Testing in Support of the Design of the NASA Composite Crew Module

Sotiris Kellas & Wade Jackson
NASA LaRC, Hampton, VA 23681

John Thesken
NASA GRC, Cleveland, OH

Eric Schleicher & Perry Wagner
ATK, Space Systems INC, Beltsville MD

Mike Kirsch
NASA LaRC, Hampton, VA 23681

Abstract

In January 2007, the NASA Administrator and Associate Administrator for the Exploration Systems Mission Directorate chartered the NASA Engineering and Safety Center (NESC) to design, build, and test a full-scale Composite Crew Module (CCM). For the design and manufacturing of the CCM, the team adopted the building block approach where design and manufacturing risks were mitigated through manufacturing trials and structural testing at various levels of complexity. Following NASA's Structural Design Verification Requirements, a further objective was the verification of design analysis methods and the provision of design data for critical structural features. Test articles increasing in complexity from basic material characterization coupons through structural feature elements and large structural components, to full-scale structures were evaluated. This paper discusses only four elements tests three of which include joints and one that includes a tapering honeycomb core detail. For each test series included are specimen details, instrumentation, test results, a brief analysis description, test analysis correlation and conclusions.

1. INTRODUCTION

During the development of the CCM, analysis and manufacturing processes were supported by a series of element-level tests. Areas of increased complexity and/or analytical uncertainty were isolated and investigated in more detail through the fabrication of representative test samples. Each element test was accompanied by a corresponding test plan and a unique set of fabrication drawings. In addition to test-method related information, each element test plan also contained analysis predictions for expected failure mode and ultimate failure loads.

For all element test analysis models FEMAP™ was employed for pre- and post-processing and MSC or NX NASTRAN® was used for the solution sequences. General finite element model checks were common to all CCM analysis models and are described in more detail in Reference [1].

Of particular importance was the element size of the 3D meshes where adhesive stresses were extracted. Unless otherwise specified, the element in-plane dimensions were held to less than 20 times the thickness, and stresses and strains were always extracted at the element centroid.

Composite ply and adhesive material strength properties and discussion on how the failure theories were implemented in the analyses, can be found in Reference [1]. For composite strength, the minimum reported values were employed in combination with the chosen failure criterion and knockdown factors References [1 & 2]. For composite ply Young's moduli E_1 and E_2, the nominal reported values were used. Unless otherwise specified, in all analyses the average of tension and compression value for Young's modulus was used. For the aluminum core, elastic and strength properties that were published by the manufacturer were used in the analyses.

This paper discusses only four element tests three of which include joints and one that includes a tapering honeycomb core detail. Tests that are discussed include the "main splice joint", the "LIDS/tunnel joint", the "core taper", and the "Titanium cruciform joint". Each test series is presented in a separate section, which includes specimen details, instrumentation, test results, a brief analysis description, and test analysis correlation.

2. MAIN SPLICE JOINT

The CCM was manufactured in two halves that were spliced together using an out-of-autoclave circumferential splice. The splice consisted of two distinct areas - the acreage and the longeron. Representative splice coupons were fabricated and tested for both regions. The purpose of the test was to verify that splice met or exceeded the minimum strength margin requirement and to provide data for analytical prediction validation.

2.1 Specimen Geometry

Specimen dimensions, for both acreage and longeron samples, are summarized in Table1. Test section is defined as the distance between the tab ends and is shown in Figure 1. For all samples, the aluminum core thickness was 25.4 mm.

The acreage specimen facesheets consisted of four fabric plies, arranged as: $[(\pm45°)/(0°/90°)]_s$. The splice laminate consisted of two fabric plies at ±45° and three plies of unidirectional tape, arranged as $(\pm45°)/0°/0°/0°/(\pm45°)$. The longeron specimen facesheets consisted of 14 fabric plies arranged as $[(\pm45°)/(0°/90°)/(\pm45°)/(0°/90°)_2/(\pm45°)/(0°/90°)]_s$. The splice laminate consisted of 12 plies, four fabric plies at ±45° and eight plies of unidirectional tape, arranged as $[(\pm45°)/0°/0°/0°/(\pm45°)/0°]_s$.

Splice specimens were fabricated in two distinct groups. For the first group (G1) of samples the two splice pieces were applied at the same time. For the second group (G2), each splice piece was cured and applied in a separate step to better simulate the actual full-scale fabrication processes. A total of seven acreage coupons (three from G1 and four from G2) and a total of five longeron splice coupons (one from G1 and four from G2) were tested. With the exception of the splice curing method, specimens in G1 and G2 were otherwise similar.

Table 1. Splice test coupon summary

Joint Configuration	Length, mm	Width, mm	Test Section, mm
Acreage	612.1	76.20	378.5
Longeron	861.8	76.20	466.1

2.2 Instrumentation and Loading

In preliminary tests, also referred to as group 1 (G1), splice specimens were instrumented with ten strain gages as shown in Figure 1. Some specimens were also speckled to enable full-field strain measurements using photogrammetry.
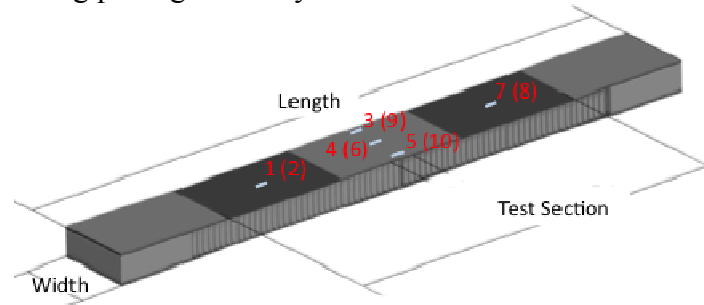

Figure 1. Specimen geometry and strain-gage positions. Gage numbers in parenthesis were located on the opposite surface.

Test coupons were loaded in tension at a constant displacement rate of 1.3 mm/minute. The force, crosshead deflection, and strain data were acquired at a rate of 5 Hz.

2.3 Test Results

Splice test results from 12 samples are summarized in Table 2.

Table 2. Summary of failure loads and failure modes

Specimen Identification	Failure Load, kN	Aver. Fail. Load, kN SD, kN	Failure Description
Acreage Specimens			
G1_001	88.90		Net-section facesheet
G1_003	94.40	92.75	Net-section facesheet
G1_004	94.96	3.35	Net-section facesheet
G2_013	61.95		Net-section facesheet
G2_014	85.37	81.48	Net-section facesheet
G2_015	90.80	13.21	Net-section facesheet
G2_016	87.81		Net-section facesheet
Longeron Specimens			
G1_004	297.7	297.7	Splice/facesheet disbond
G2_006	332.5		Splice/facesheet disbond
G2_007	347.3	349.7	Splice/facesheet disbond
G2_008	365.8	13.8	Splice/facesheet disbond

G2_009	353.1		Splice/facesheet disbond

The failure mode for all seven of the acreage-splice coupons was a net section failure of the facesheet. The failure mode for the five longeron coupons was an adhesive failure between the splice and the facesheet.

2.4 Analysis

The model used for the splice test was a 3D ply-by-ply model. Each facesheet and splice ply was modeled with at least one element through the thickness. Some plies were modeled with two elements through the thickness to allow for additional mesh refinement. Due to symmetry, only half of the specimen was modeled. Load was applied at the surface nodes of the end-tab elements. The composite blocks at the ends of the specimen were represented by a single through-the-thickness element with assumed quasi-isotropic properties. The bond between the end-tabs and the facesheet was modeled as a discrete layer containing one element through the thickness.

The center of the specimen, where the two sandwich panels came together had an intentional space of 2.54 mm to represent possible gaps during the mating of the two full-scale CCM halves. In the test specimens, this gap was filled with EY3010 potting compound to effectively transfer shear from one panel to the other. It was postulated that prior to ultimate coupon failure, this bond would crack and therefore, in the model the potting compound was released from the splice and the facesheets.

Consistent with the full-up CCM analyses, pre-test finite element analysis utilized the average of tension and compression E_1 and E_2 for the composite plies, which resulted in conservative predictions. Post-test analytical predictions were updated to better match the tensile test condition. Both E_1 and E_2 input values corresponded to the tensile values. Because the strain-to-failure remained the same, the increase in stiffness input value resulted in slightly higher strength predictions. Two possible modes of failure were investigated; bond failure between the doubler and the sandwich panel, and net-section failure of the sandwich panel termed "facesheet failure". A summary of post-test analytical prediction ranges together with the associated modes of failure is shown in Table 3. For the acreage splice, the predicted facesheet failure range was lower than the bond strength range, whereas for the longeron case the two modes of failure overlapped.

Table 3. Post-test analytical prediction ranges

Acreage Splice		Longeron Splice	
Bond Failure Range, kN	Facesheet Failure Range, kN	Bond Failure Range, kN	Facesheet Failure Range, kN
106.3 – 157.6	64.41 – 96.57	284.5 – 387.4	231.7 – 347.5

2.5 Test/Analysis Correlation

A typical strain response comparison between analysis and test are presented in Figure 2 for an acreage splice sample. Corrected stiffness values were used in these analytical predictions.
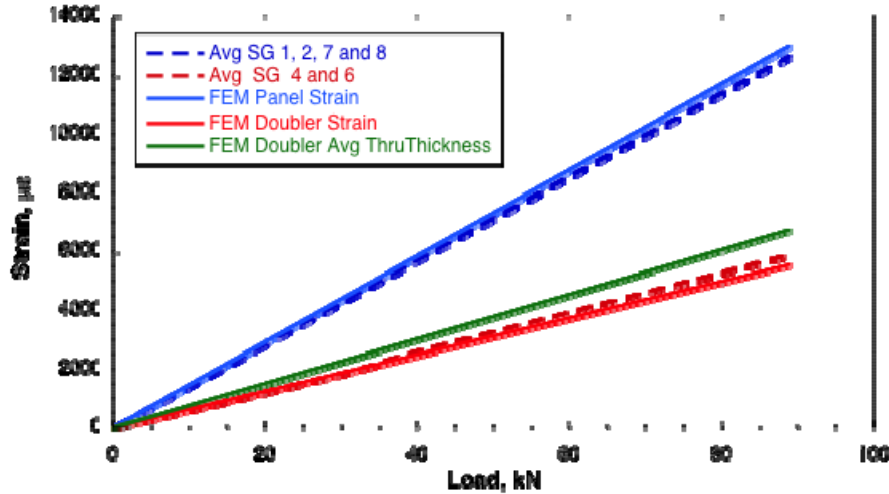
Figure 2. Comparison of post-test analytical and experimental strain-gage responses for the acreage splice sample 001

In general, strain predictions for the acreage splice correlated well with measured strain responses. The greatest deviations were for the strain gages located in the center of the doubler with a maximum difference of about 5.5 %. The difference between test and analysis for the center strains could be attributed partly to potting compound cracking at the edge of the facesheet. In the finite element models (FEM) this bond showed high stresses; however, since it is not a load-carrying bond the stresses were ignored. Figure 3 shows a FEA model of the test sample and a close up edge view of the deformed mesh around the broken bond.

As seen in Figure 3, the FEA model predicts localized bending in the center of the doubler as it bridges the gap between the facesheets. For the acreage splice, the magnitude of the analytical bending strain was 2380 $\mu\varepsilon$, or 33 % of the membrane strain. Bending in the doubler was found to depend on (a) the gap size between the two facesheets (shown in red), the smaller the gap the lower the doubler bending (b) the relative stiffness between the facesheets and splice laminates which controls the magnitude of the bending moment generated by the load eccentricity and (c) the thickness of the doubler which controlled the degree of eccentricity. Since maximum bending occurs at the center of the gap, it is anticipated that the measured strains also depend on the exact positioning of the strain gage – a higher strain is expected if the strain gage happened to be off center.
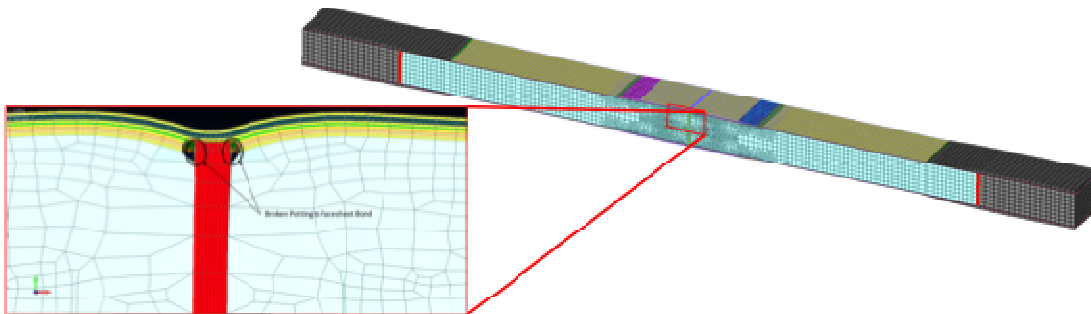

Figure 3. Close up view of the deformed mesh at the center section of the specimen. Deformations are not shown to scale.

For the longeron splice, the effect of bending was more obvious. In this case, the predicted bending strain in the center of the splice was 4628 με, or 65 % of the membrane strain. Consequently, a third possible mode of failure in the longeron samples, dependant on the integrity of the potting compound, was tensile failure initiating in the innermost ply of the splice laminate due to localized bending. Assuming complete loss of integrity of the potting compound, the predicted splice tensile failure was estimated at 272.2 kN. Even though this tensile-type of failure was 4.4 % lower than the lowest predicted bond failure, none of the longeron samples failed in this mode, proving that some residual potting integrity.

As predicted all acreage samples failed by facesheet fracture, away from the spliced region, and except from sample 013 all other samples failed within the expected range. All longeron samples failed in the splice section by sandwich panel/doubler separation. All samples exhibited strengths within the predicted range.

3. LIDS/TUNNEL JOINT

The Low Impact Docking System (LIDS) is a metallic interface ring. For the CCM, the LIDS ring was fabricated out of aluminum that was paste bonded to the cured CCM tunnel and further reinforced by the addition of a six-piece composite doubler. In essence, the addition of the doubler transformed the joint from a lap shear to a double shear joint. The location of the LIDS ring on the CCM and structural details of the joint are shown in the schematic of Figure 4.
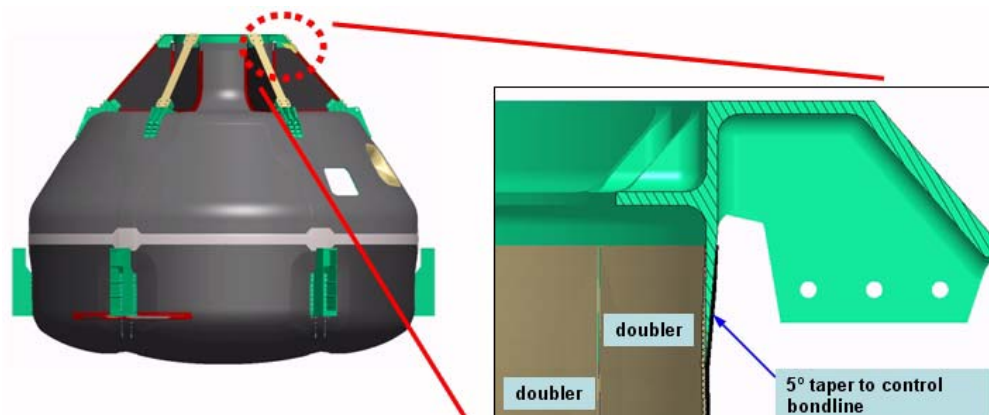

Figure 4. Schematic of LIDS ring/tunnel interface joint (LIDS ring is shown in green and the composite doubler is shown in light brown)

The objective of the element test was to evaluate the strength of the LIDS ring/tunnel joint using a simplified test article and to provide data for analysis correlation.

This test was guided by Reference [3], which in addition to test configuration included the pre-test results from a linear elastic analysis. Specimen design was based on the pre-test linear elastic analysis. Following the test, it became apparent that the asymmetric geometry of the specimen led to non-linear geometric response that was not properly captured by the linear

elastic FEA. Therefore, post-test analysis was updated to provide a geometrically non-linear solution.

3.1 Specimen Geometry

Specimen geometry is shown in Figure 5. The specimen consisted of an aluminum adherend representing a section of the LIDS ring, a composite adherend representing the solid laminate of the composite tunnel and a third laminate representing the composite doubler. Composite end-tabs were added to the composite end of the specimen to accommodate grip loads. The grip end of the aluminum adherend was machined eccentrically to minimize specimen bending.

The nominal thicknesses in the test gage section of the aluminum and composite adherends, were 6.35 mm and 2.06 mm, respectively. These thicknesses were tapered down to a knife-edge in the bonded joint region. The adhesive thickness was controlled to 0.38 mm. Due to material availability, the as-manufactured length of the aluminum adherend for the specimens was 12.7 mm shorter than specified by the drawings.
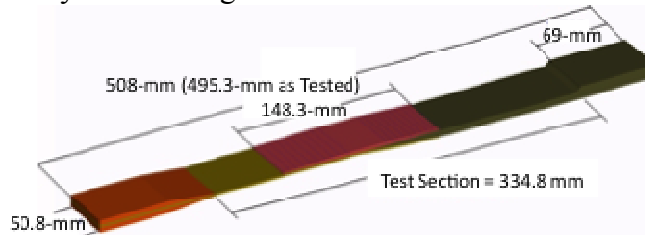

Figure 5. Specimen geometry. As built sample length was 12.7 mm shorter than drawing.

3.2 Instrumentation and Loading

The instrumentation, defined in the test plan Reference [4], was modified to eliminate two of three back-to-back pairs of foil strain gages. Instead, full-field photogrammetry was used to study the deformation and strain distribution around the joint region. The speckled pattern for the full-field strain measurement covered the doubler and one profile edge of the specimen. Bending in the composite adherend was measured by a pair of back-to-back strain gages, located along the specimen symmetry line halfway between the edge of the end tab and the edge of the doubler.

Load, cross-head displacement, and strain gage measurements were recorded at 6 Hz. Load was applied under displacement control with a constant displacement rate of 3.2 mm/minute.

3.3 Test Results

Measured strength, maximum cross-head displacements and maximum strains are summarized in Table 4 and deduced properties such as global specimen stiffness and Young's modulus of the composite adherend are summarized in Table 5. Averaged values together with the corresponding standard deviation are also shown in these tables.

Test section was defined as the specimen-free length between the machine grips, and cross-head displacement was the elongation of that gage length. The specimen stiffness was determined by

a least square fit of the measured load versus cross-head displacement slope. Full-field optical strain measurements were used to capture the strain distribution on the doubler midline near the aluminum knife-edge and along the end of the doubler attached to the composite adherend. The average of the strain gage pair was used to estimate the membrane strain in the composite adherend. This was used in conjunction with the measured cross-section of the composite adherend in this location to compute an effective elastic modulus for the composite adherend.

A typical full-field strain at ultimate load is shown superimposed on the actual specimen in Figure 6. Three faint horizontal grey lines, drawn on the specimen, define the edges of the composite doubler and the position of the aluminum knife-edge covered by the doubler. It was clear that the strains at the edge of the doubler bonded to the composite adherend were the highest reaching nearly 1.0 % strain, while the strains at the midline near the aluminum knife-edge were about one tenth in magnitude and uniformly small in the midsection of the composite doubler.

Table 4. Summary of measured strength and strain at failure

Spec. No.	Max Load, kN	Displ., mm	Doubler Strain[1], %	Doubler Strain[2], %	Comp. Adherend Strain[3], %
1	42.57	1.65	0.169	1.096	0.877
2	35.40	1.40	0.107	0.833	0.735
3	44.20	1.75	0.167	1.288	0.904
4	51.37	2.01	/[4]	/	1.040
5	37.25	1.50	0.131	0.917	0.800
6	40.50	1.60	0.134	/	0.853
7	40.07	1.60	0.132	1.008	0.822
8	41.48	1.91	0.188	1.075	0.837
Aver./St.D	41.60/4.84	1.68/0.20	0.1470.028	1.036/0.158	0.859/0.089

Table 5. Summary of stiffness calculations from experimental measurements

Spec. No.	Test Section, mm	Specimen Stiffness, kN/mm	Comp. Adherend Modulus, GPa
1	364.7	25.9	50.5
2	363.2	25.6	50.1
3	363.7	25.6	50.2
4	363.2	25.6	49.2
5	359.9	24.9	47.2
6	360.2	25.7	48.1
7	359.9	25.6	49.9
8	358.9	25.4	52.3
Average / St. Deviation		25.5 / 0.31	49.7 / 1.55

[1] Full-field optical strain measured at the mid-line.
[2] Full-field optical strain measured at the end.
[3] Average of strain gages.
[4] Due to excessive noise to signal ratio, meaningful values could not be extracted.

Quantitative data at discreet locations were extracted by establishing "stage points" in the photogrammetry images. The group of stage points along the edge of the composite doubler was used to compute an average value of strain at the doubler edge for each specimen in Table 4. It is worth noting that only tensile axial strains were found on the doubler over the entire field of measurements and the extreme strains at the knife-edge of the doubler were about four to seven times the magnitude of the mid-line (center) of the doubler.

Except for one specimen where the composite doubler remained bonded to the aluminum part, all specimens failed in three separated pieces. Post-test inspection of the adherends and doubler revealed a typical pattern of adhesive failure along the adhesive-adherend interface. The aluminum adherends were generally fully covered on each bond surface with adhesive. All fully separated doublers were covered with adhesive on the part of the doubler that bonds to the composite adherend. At the aluminum knife-edge, the adhesive was observed to fracture normal to the load direction leaving the doubler completely free of adhesive on the surface that bonds to the aluminum adherend.
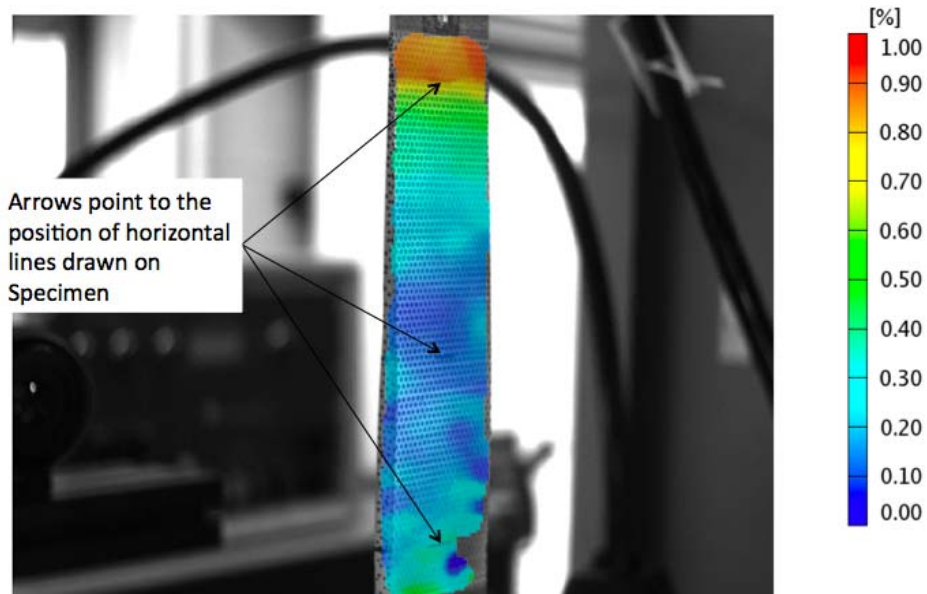

Figure 6. Typical full-field axial strains superimposed on actual specimen (image shown close to the failure load for specimen 2)

Given that one specimen was left with the doubler/aluminum bond intact, this suggests that the failure process initiates on the composite adherend interface. The full-field strain measurement showed that the greatest deformation occurred at the doubler/composite adherend interface suggesting that the doubler/composite interface might be the likely weak link.

3.4 Analysis

The test coupon was modeled using 3D elements. The composite section of the specimen consisted of ten 0.21 mm thick fabric plies. Each ply was modeled with one through-the-thickness element.

The end-tabs on the composite end of the specimen consisted of multiple plies of fabric cured and then machined to the final size and bonded to the laminate. In the model, this was represented by a single element through the thickness with quasi-isotropic properties. A single layer of elements modeled the bond between the end-tabs and the tunnel laminate.

The composite doubler, which consisted of a combination of unidirectional and fabric plies, was also modeled ply-by-ply. The fabric plies were 0.21 mm thick and the unidirectional plies were 0.135 mm thick. The paste bond between the doubler and the tunnel laminate was modeled with a 0.381 mm-thick element. The bond of the doubler and the tunnel laminate to the aluminum LIDS ring was modeled using the same technique.

All failure loads fell within the prediction load range of the pre-test analysis. However, it should be pointed out that these predictions were based on pre-test linear FEA that did not represent the as-tested specimen length. As a result, the measured specimen gage length deflections (shown in Table 4) are a factor of two smaller than the predicted 3.05 mm. Moreover, the corresponding specimen stiffness was found to be about 50 % greater than what is shown in Table 5. Therefore, a post-test geometrically nonlinear FEA was performed with the as built specimen length to account for the out-of-plane deformations. Paste-bond failure was found to be possible in the load range between 38.81 and 82.63 kN and composite adherend failure was found to be possible in the load range of 37.56 to 56.35 kN. Data from the updated model were used to correlate with the experimental results as described in the following section.

3.5 Test/Analysis Correlation

A summary of the stress as a function of the nominal composite adherend strain is shown in Figure 7. The nominal composite adherend strain is the membrane strain found by taking the average to the back-to-back strain gages. The experimental responses are compared to the post-test nonlinear FE results. For the analysis, strains were extracted at the strain gage position. The results of Figure 7 demonstrate an excellent agreement between the FEA model and the far field stress/strain response. The effective modulus of the composite section of the specimen was found to be within 1.0 % of the average of the measured values reported in Table 5.
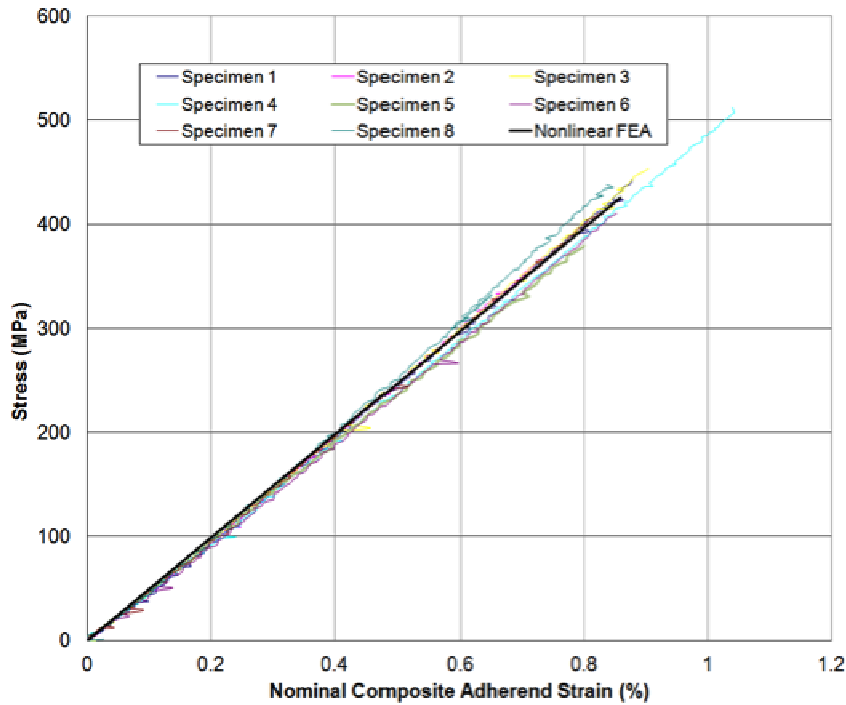
Figure 7. Comparison of experimental stress versus strain to nonlinear FEA response. To obtain stress, the applied load was divided by the cross-sectional area at the strain-gage location

In addition to strain measurement, photogrammetry provided out-of-plane displacements, which were used to examine the out-of-plane bending response relative to the nonlinear FE results. Figure 8 compares the nonlinear FEA results to the load as a function of the out-of-plane displacement results for two locations: doubler edge and midline of the doubler. The measured data show that the out-of-plane deflection at the doubler knife-edge asymptotically approaches a maximum of about 1.02 mm. This is greater than the nonlinear FEA result (red trace), which decreases in magnitude after reaching a maximum of about 0.74 mm.

With the exception of sample 8, the out-of-plane displacement measured at the midline, also appears to tend towards an asymptote at approximately 1.78 mm as compared to an approximate asymptotic value of 1.32 mm obtained from the nonlinear FEA results.
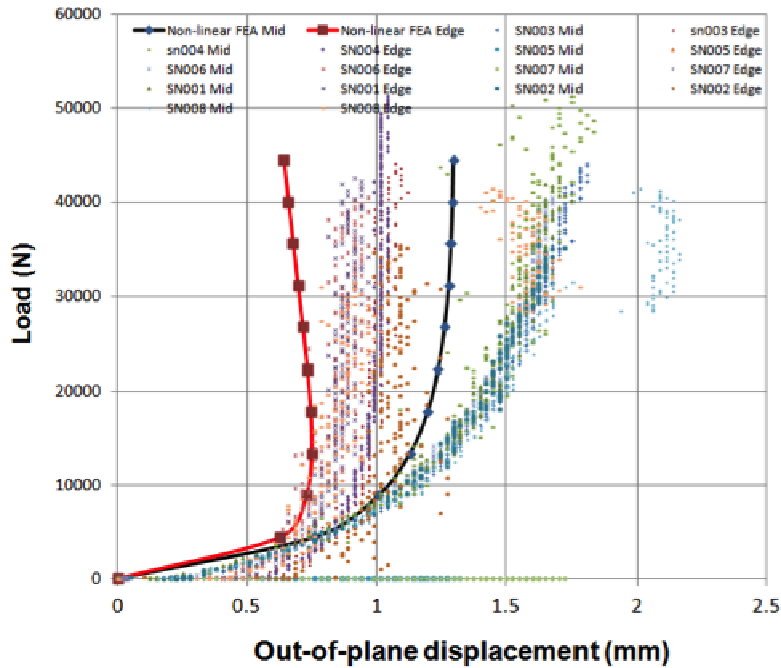
Figure 8. Measured versus analytical out-of-plane bending response.

Since the rate of deformation decreases with increasing load it may be concluded that the asymmetric coupling is functionally dependent on load. Further calibration of the nonlinear FEA model is likely required to match the localized strain measured at the doublers midline more accurately. With this in mind, the current nonlinear FEA results have been used to determine an updated ultimate flight load design margin calculation given in Table 6. Three additional pieces of information were used for this calculation: maximum doubler strains, the peak paste bond normal stress, and shear stress.

The margin calculations, based on the material allowables, are summarized in Table 6. The results show that the paste bond has the highest strength margin. However, based on previous work with paste-bonded structures, Reference [5], a large strength scatter was anticipated and is supported by the paste-bond failure observed in all specimens.

Table 6. Margin of safety calculation for the 5.83 kN flight load using the nonlinear FEA results

Location	Mode Of Failure	Stress/Strain (Ultimate at Location)	Factor of Safety	Margin
Tunnel	Tension/ Bending	1402 µe	2.0	+ 2.88
Doubler	Tension/ Bending	1205 µe	2.0	+ 3.52
Paste Bond	Tension/Shear Interaction	Shear = 3.21 MPa Tension = 4.52 MPa	2.0	+3.89

The predicted paste-bond failure ranged from 38.81 to 82.63 kN and the predicted composite adherend failure ranged from 37.56 to 56.35 kN. Based on these ranges, the net section composite failure mode was predicted to be the most likely failure mode. While the average experimental strength of 41.61 kN was within the predicted failure band, two specimens, 2 and 5, failed at a load below the minimum strength prediction of 37.56 kN.

4. CORE TAPER

The CCM structure utilized core tapers at every major bolted fitting location. In those regions the core thickness was gradually reduced to transition to a solid laminate. Preliminary structural analysis indicated that the core shear strength design allowable was reached or exceeded in many core-tapered regions of the structure, which inevitably prompted this study. To investigate the effect of exceeding the core design allowable on sandwich structural integrity and to validate modeling techniques, a simple test article was devised and tested in three-point-bending.

The objective of the test was simply to determine whether catastrophic failure would occur when the core design allowable, as predicted by linear FEA models, was exceeded. During the preliminary phase of this test program, samples were tested with the flat facesheet in either compression or tension. In this paper, only the results from the specimens that were loaded with the flat face sheet in tension are presented. This loading configuration, shown schematically in Figure 9, was representative of the full-scale structure. Test details, including pretest predictions, and preliminary test results are described in References [6 & 7].

4.1 Specimen Geometry

The core-taper geometry was determined by the full-scale structure construction. The specimen's facesheet stacking sequence and thickness were tailored such that the core shear strength design allowable would be exceeded prior to facesheet/core debonding and/or fracture. Specimen width was 50.8 mm with nominal facesheet thickness of 3.92 mm. Each facesheet consisted of eleven 0.36 mm-thick fabric plies oriented at 45°/0°/0°/-45°/0°/0°/0°/-45°//0°/0°/45° with the 0° being along the beam length. The core was aluminum honeycomb with density of 70.5 Kg/m^3. The ribbon direction of the core was oriented along the specimen length. A solid block of graphite/epoxy was molded at the center of the coupon, as shown in Figure 9, to provide a hard point for load application and to preclude core failure outside of the core ramp.
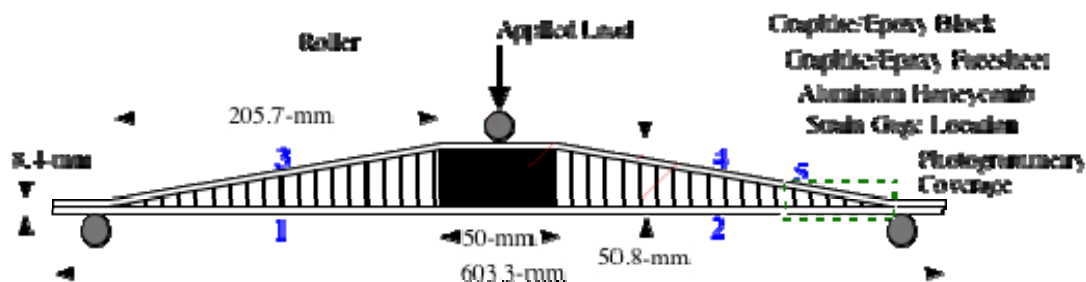

Figure 9. Sample geometry and location of instrumentation. (Strain gage locations are indicated by numbers 1−5)

4.2 Instrumentation and Loading

Preliminary tests were performed without end tabs, however, to better simulate the clamp-up pressure that the bolted fittings provide in the solid laminate of the panned down regions of the CCM, the remaining samples were tested with metal end-clamps as shown in Figure 10.
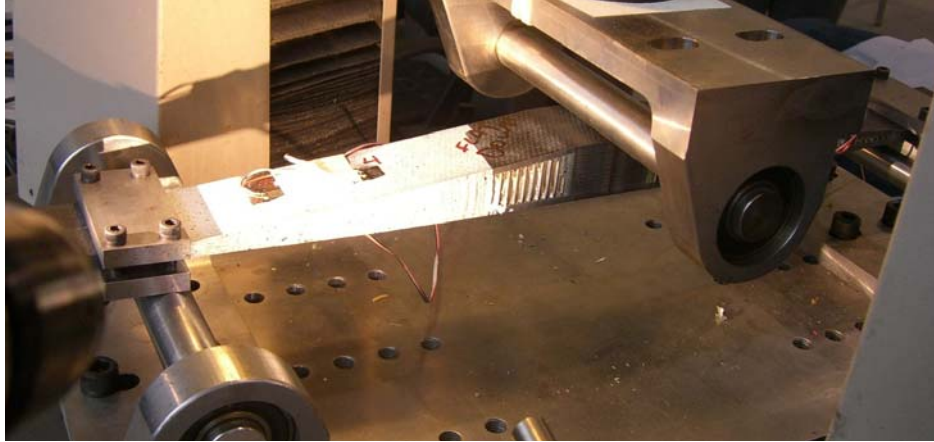

Figure 10. Photograph of sample tested with end tabs. (Also shown is the photogrammetry speckled pattern)

One specimen end was speckled for photogrammetric measurements. Prior to painting, the exposed honeycomb core edge was filled with a low modulus latex-based caulking material to provide an even surface. The painted end is shown in Figure 10.

4.3 Test Results

For the loading configuration with the flat facesheet in tension, one sample, specimen 2, was loaded without end tabs and two samples, 5 and 6, with end tabs (clamped ends). The average ultimate load for the clamped end configuration was 10.19 kN. The mode of ultimate failure for both clamped samples was debonding of the top facesheet, as shown in Figure 11. Compared to the specimen without end tabs, clamped specimens exhibited an increase in ultimate load of 16.3 %.

Figure 11. Photograph of the failed end of test coupon with clamped ends

Average mid-span facesheet strains as a function of applied load are presented for the load case with and without end-tabs in Figure 11. For clarity, the response of sample 5, which was similar to that of sample 6, was omitted.
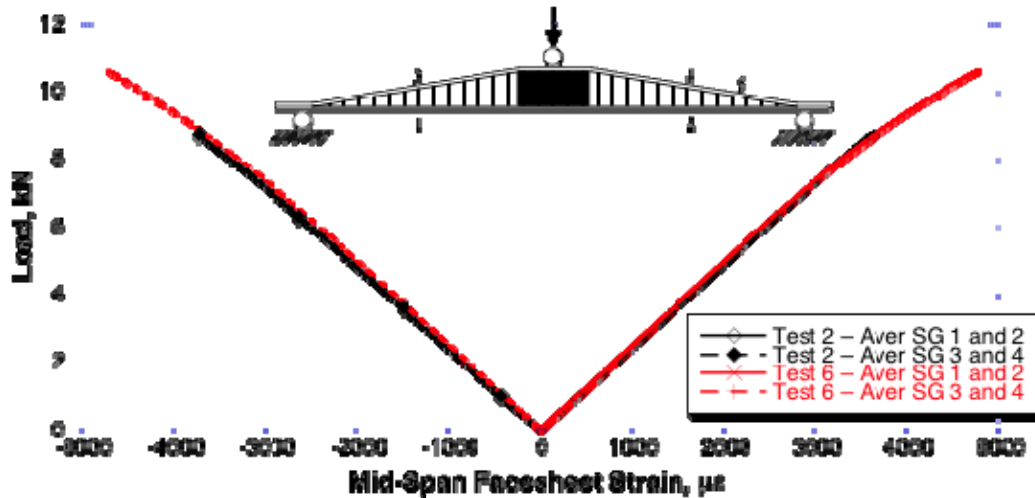
Figure 11. Facesheet strain versus applied load for specimens with and without clamped ends. Strains are the measured average values from top and bottom center span strain gages.

Figure 11 shows that the strain responses for the two loading cases (with and without end-tabs) are relatively linear and similar to each other in the range of load up to 8.76 kN—the failure load of sample 2.

Shear strain measurements which were used for test analysis correlation, were obtained from the full-field measurements. Photogrammetry measurements were taken both on the top facesheet as well as on the specimen edge. The accuracy of the photogrammetry measurements was assessed by comparing the strain reading of gage 5 to a nearby "virtual gage". A best polynomial fit to the digital strain results against the nearby strain gage response is shown in Figure 12. Results show good correlation between the strain gage and the digital gage for up to a load of 4.89 kN, or -0.152 % strain. Beyond 4.89 kN, photogrammetry underestimated the strain with the largest measured deviation being only 3.4 % at 9.84 kN.

An example of full-field shear strain is shown in Figure 13. From the strain field of Figure 13, shear strains at discrete points were extracted along a vertical line, shown in yellow, and plotted in the form of strain versus through-the-thickness position in Figure 14. The through thickness shear strain response resembles a parabola with the peak occurring roughly midway between the top and bottom facesheets as expected. However, accurate measurement of the shear strain magnitude in the core was complicated due to the uneven surface of the honeycomb and the uncertainty of the effect of core filler. Therefore, an indirect measurement of the average shear strain in the core was obtained based on the relative displacements of the facesheets.
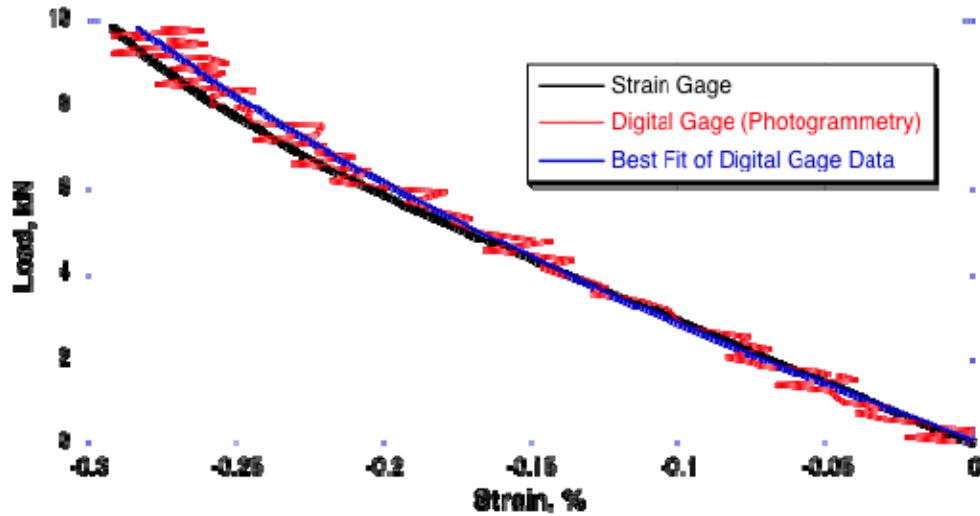
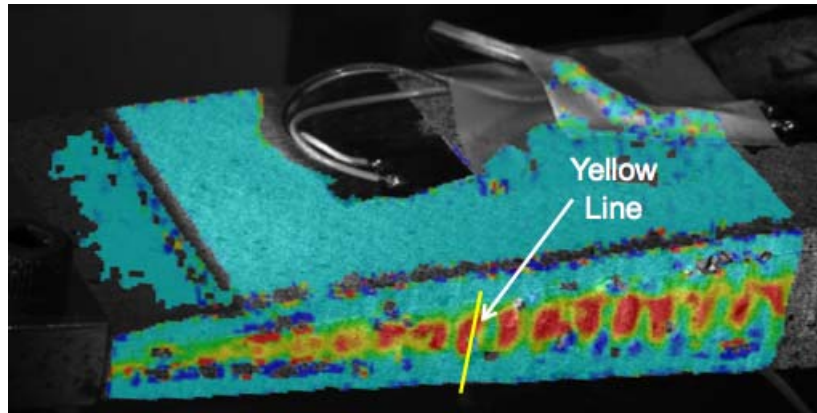Figure 12. Strain gage versus photogrammetry based strain measurements for sample 5

Figure 13. Typical example of full-field strain for Sample 5 at ultimate load (shear strain distributions were extracted along the yellow line and are presented in Figure 14.

For this indirect calculation the shear strain, γ, was related to the rate of change of deformations using Equation 1. Displacements were tracked at four reference points located on the facesheets of sample 5 and are shown in the inset of Figure 15. This calculation produced an average shear strain through the thickness of the core. A plot of the average through-the-thickness shear strain versus load is presented in Figure 15.
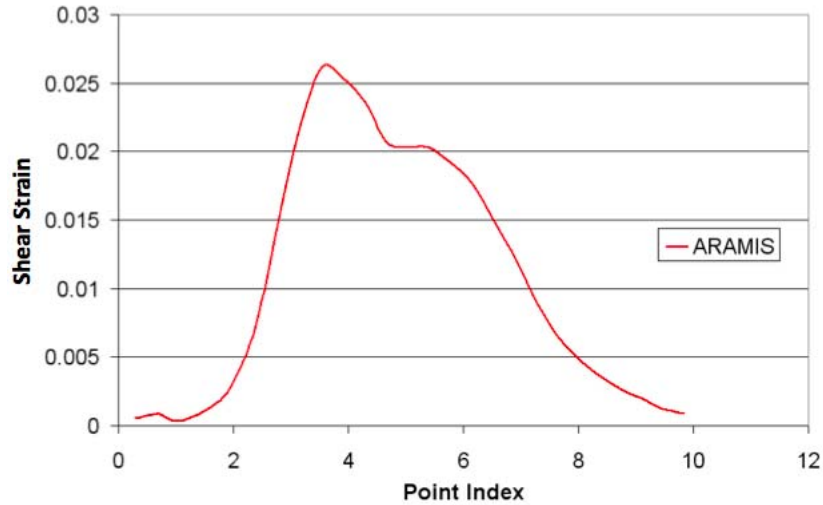
Figure 14. Shear strain versus through-the-thickness position for sample 5 at 9.84 kN

$$\gamma(x) = \frac{\Delta u_x}{\Delta y} + \frac{\Delta u_y}{\Delta x}$$
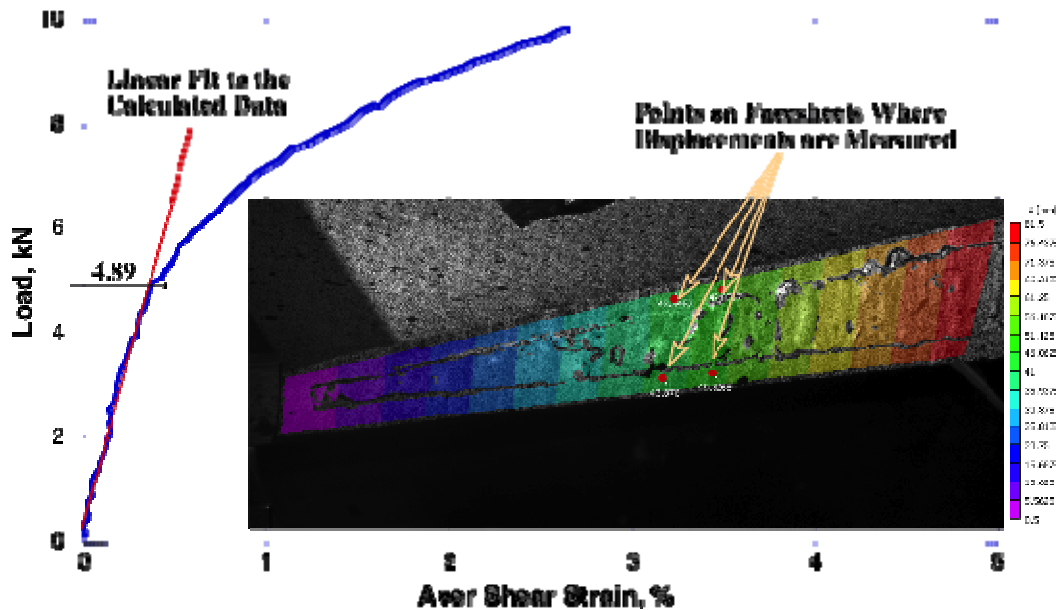
(1)

Figure 15. Average core shear strain as a function of load

Through non-linear in its entirety the load/shear-strain response of Figure 15 appears to become progressively more non-linear at higher load. In particular, the response appears to deviate from a linear fit of the initial portion of the data at approximately 4.89 kN. The decrease in the core shear stiffness is most likely associated with the initiation of shear yielding and/or cell shear buckling (wrinkling of the cell walls).

4.4 Analysis

The FEA modeling approach common to the CCM project was followed for this element test. In the pre-test analysis, the core was represented with solid elements with homogenized properties, and the composite facesheets were modeled with shell elements.

As shown in the FEA core shear strain distribution in Figure 16, peak shear stress occurred at the core knife-edge. At 6.23 kN of applied load, nearly one quarter of the core ramp had reached the shear stress allowable of 2.28 MPa (330 psi).
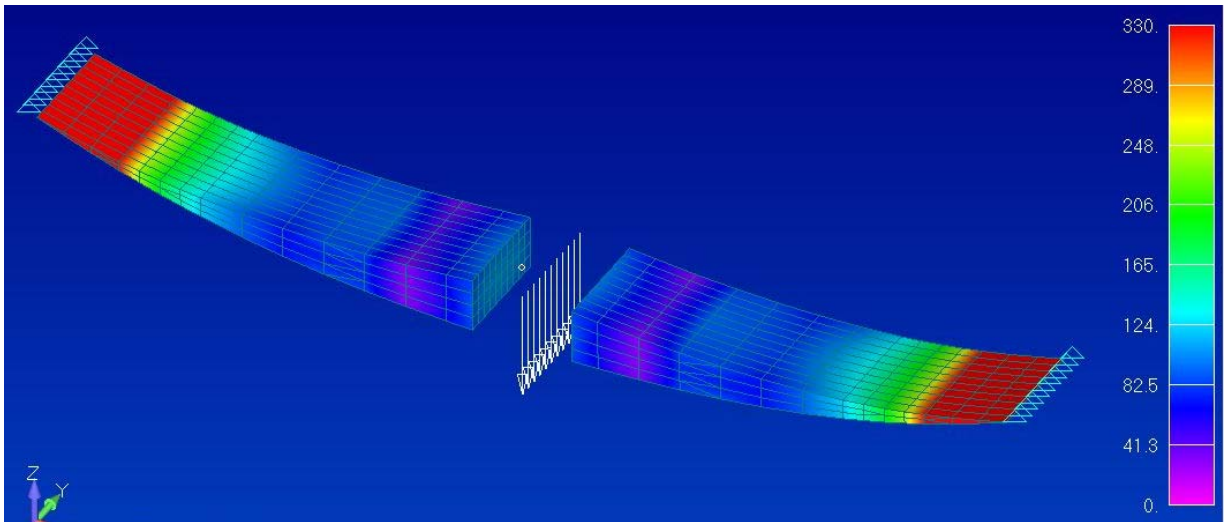

Figure 16. Shear stress distribution in the core at an applied load of 6.23 kN. Elements in red (at the knife-edge) are at the core allowable value

4.5 Test/Analysis Correlation

Test/analysis correlations of tensile mid-span axial strains (at positions 1 and 2) for sample 5 and 6 are shown in Figure 17. Compared to the corresponding FEA strain, Figure 17 shows a good correlation between measured and predicted strains at the mid-span. Moreover, the responses of Figure 17 show that the facesheet strain responses remain linear beyond the load of approximately 4.89 kN where a deviation from linearity was observed in load/shear strain response of the core. A similar result was also true for the facesheets in compression (strain gage positions 3 and 4).
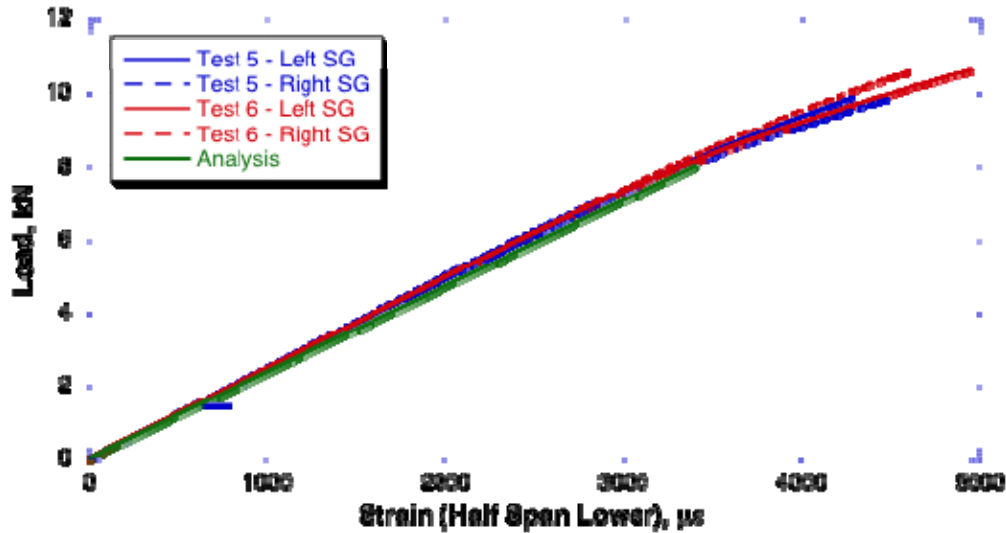
Figure 17. Test versus analysis at strain gage positions 1 and 2

Based on core shear strength allowable, pre-test analysis predicted that the core at the knife-edge would exceed the design allowable when the applied load reached 5.34 kN. As shown in Figure 16, at 6.23 kN of applied load nearly one quarter of the core up the ramp has reached the design allowable. However, experimental results showed that specimens were capable of carrying load in excess of 9.79 kN.

Physically, as the core becomes less effective in carrying shear, load can be shunted to the facesheets, which can accommodate additional deformation before catastrophic failure occurs. However, it is postulated that the degree to which load can be carried by the facesheets, past the core design allowable, depends on the thickness of the facesheets and the core taper geometry.

While determining the exact load at which the core shear strength allowable was reached was not possible, Figure 15 shows that at approximately 4.89 kN and above the load versus average through-the-thickness shear strain response began to deviate from linearity.

5. TITANIUM CRUCIFORM

The CCM's structural backbone assembly consists of nine individual composite sandwich panels, which made up the main keel beam (three pieces), the two rib beams (four pieces) and the two stub keels (two pieces). Originally, the backbone intersections, where the four composite beam sections come together, were to be integrated together using a titanium cruciform (a four sided clevis). The intention was to paste-bond the four pre-cured sandwich panels into the clevises of the titanium cruciform.

The main objectives of the element test were (a) to measure the strength of the joint and to verify that it met the minimum strength requirements and (b) to provide data for verification of the analysis techniques used on the full-scale backbone structure. A secondary objective was to gain manufacturing experience with the EA 9394™ paste bonded joint. More details on this test, including pre-test strength predictions, can be found in the test plan Reference [8] and the CCM final test report [7].

5.1 Specimen Geometry

A total of five cruciform samples were fabricated individually and tested. The test specimen geometry is shown in Figure 18. Each leg of the cruciform consists of a sandwich panel, representative of the corresponding backbone beam. Each piece was paste bonded into the clevis of the titanium cruciform. The free end of each leg was reinforced to accommodate grip pressure for load application. At the reinforced ends, the aluminum core was replaced with a solid graphite/epoxy composite block and the facesheets were reinforced with extra plies, tapering in thickness as they extended beyond the length of the composite block. The specimen length dimension was 489.2 mm, the height (or width of each sandwich leg) was 50.8 mm, the thickness of each sandwich leg (excluding the ends) was 26.2 mm and the end-tab insert was 50.8 mm long.

To represent the backbone construction correctly, three of the sandwich panels (branches) contained 10-ply facesheets and the fourth contained 6-ply facesheets. Consequently, tests were conducted along two orientations as shown in the schematic of Figure 19.
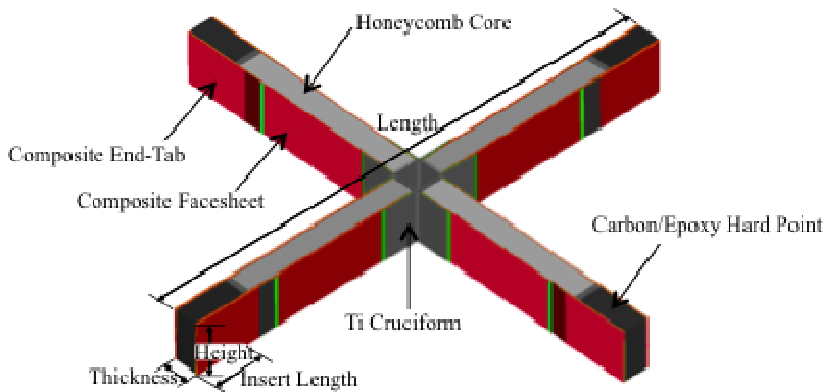

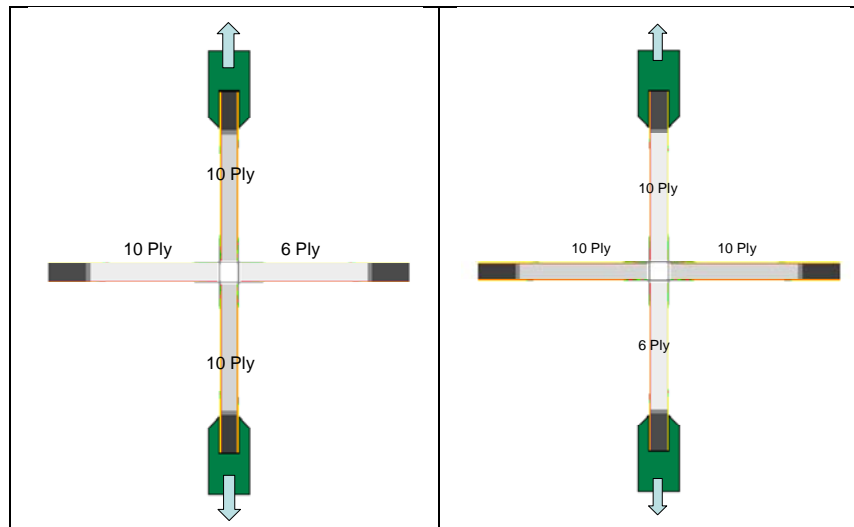Figure 18. Diagram of a cruciform specimen showing critical dimensions

Figure 19. Schematic of the two loading configurations

5.2 Instrumentation and Loading

Three uniaxial strain gages were installed on each of two orthogonal legs of the cruciform specimens – two gages were installed on one side of the leg and one on the other. Full-field strain measurements at the edge of the cruciform bond were also made using photogrammetry. Load was applied until a load drop of greater than 10 % was observed—the peak recorded load is referred to as the failure load.

For each specimen, load was applied in either or both the 10-10 and 6-10 ply directions. Analytical predictions showed that the facesheet and bond failure modes were equally likely for the 6-10 pull case and more likely to be the bond line for the 10-10 pull case. All samples were tested in tension except for a single specimen that was loaded in compression to make sure all aspects of the design were investigated.

5.3 Test Results

While most samples were tested only in one direction some samples were tested sequentially along both orientations. Tests in the second orientation after failure in the first direction were performed with the understanding that the test sample was no longer considered being in pristine condition. Often the bonds in the transverse direction of the cruciform failed due to the sudden spring back caused by failure in the loaded direction. This was the case for sample 2 as shown in Figure 20. The test sequence and test results, including loading sequence and modes of failure, are summarized in Table 7. Letters a, b and c accompanying the specimen-number correspond to first, second and third load sequence, respectively.

When the 10-10 direction was pulled first, the specimen failed in the cruciform bond as predicted. When that same specimen was then tested in the 6-10 direction it failed prematurely by bondline fracture—this indicated bond degradation due to the first pull.

The two failure modes for the 6-10 direction were facesheet fracture and failure in the cruciform bond. The two failure modes appeared to overlap. In specimens 3 through 5, where the 10-10 direction was pulled first and a failure occurred, the energy release likely caused a crack in the 6-10 direction bond line. When the specimen was then tested in the 6-10 direction, the failure would be in the joint instead of net section as it was for specimen two.

Table 7. Summary of cruciform test results

Specimen No.	Loading/ Orientation	Failure Load, kN	Facesheet strain, $\mu\varepsilon$	Failure Description
1	Compression/ 10-10	-74.18	-8,044	Ti Cruciform Shear Buckling
2	Tension/ 6-10	83.40	8,213	6-ply Facesheet Failure
3a	Tension/ 10-10	51.05	5,045	Bond Failure (Crack @ 31.58-kN)

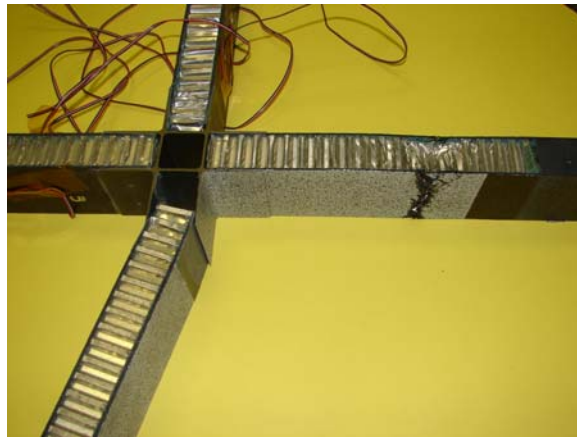|				
3b	Tension/ 6-10	34.32	3,388	Bond Failure
4	Tension/ 10-10	69.54	6,949	Bond Failure
5a	Tension/ 6-10	N/A	N/A	Proof Load to 53.38 kN No Failure
5b	Tension/ 10-10	65.72	6,525	Bond Failure
5c	Tension/ 6-10	61.12	6,041	Bond Failure

Figure 20. Facesheet failure in the horizontal leg of sample 2 when pulled along the 6-10 orientation, caused bond failure in transverse direction due to spring back

5.4 Analysis

The sandwich panels of the cruciform were modeled using a 3D mesh. A single layer of elements was used for each ply of the composite facesheets. Due to symmetry, only half of the specimen was modeled with appropriate boundary conditions. Consistent with the modeling of the CCM backbone structure, the average of tension and compression moduli, E_1 and E_2, were used for the modeling of the composite cruciform legs.

The build up for the clamped end of the panels was multiple plies of carbon fiber fabric co-cured with the facesheets. In the model, this was modeled ply-by-ply just like the facesheets. The paste bond between the cruciform and the face sheets was modeled using one element through the thickness. As shown in Figure 21, the model included the paste-bond taper and the taper at the end of each titanium cruciform leg.
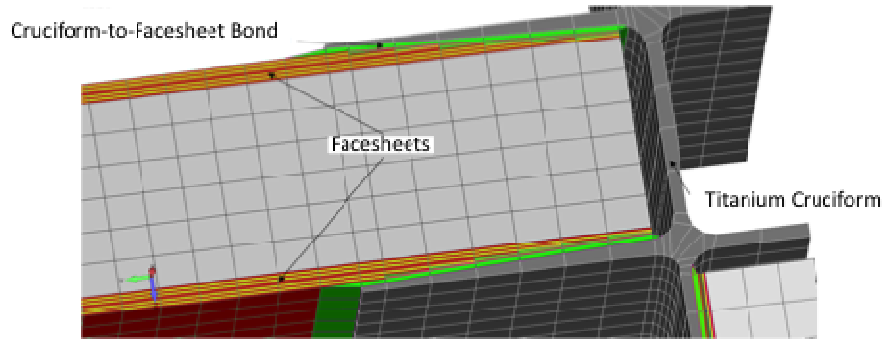
Figure 21. Close-up of facesheet to cruciform bond (paste bond is shown in green)

5.5 Test/Analysis Correlation

A comparison of predicted versus measured failure loads are summarized for both the 6- and 10-ply legs in Figure 22. In addition to the load range for each possible mode of failure, Figure 22 also shows the design strength requirement for each of the leg types.
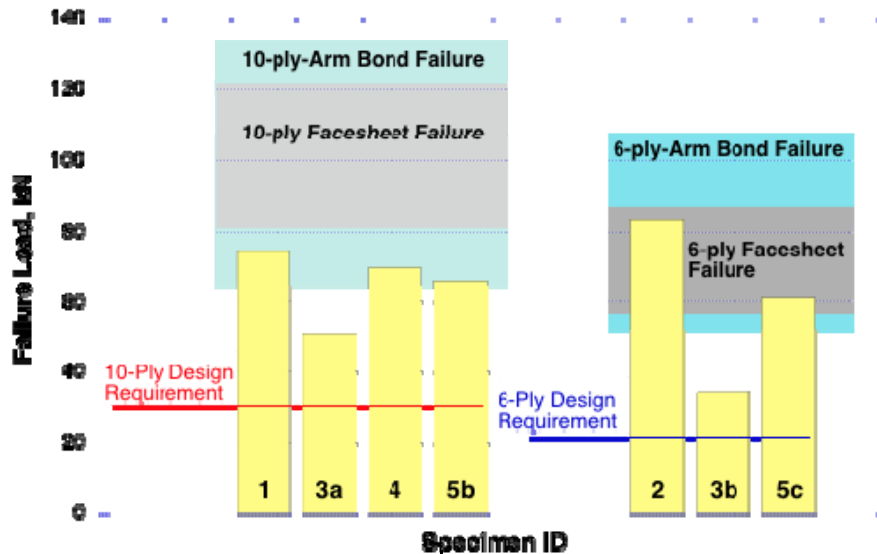

Figure 22. Predicted and measured strengths

For both the 6- and 10-ply arms, the predictions for the bond and facesheet mode of failure overlap. Consequently, in every loading case there are two competing failure modes. For specimen 2, where the pull was in the 6-10 direction, facesheet failure in the 6-ply arm occurred within the predicted range. The bond integrity for specimen 2 also exceeded the minimum bond failure predictions for both the 6- and 10-ply legs. All other tensile specimens failed in the bondline and at lower load. For these samples, the failure loads were near or below the predicted minimum bond strengths. The only pristine sample that failed below the minimum prediction was sample 3a. Test case 3a was lower than the minimum bond-failure prediction but still 67 % higher than the design allowable. The large variation in bond strength, which could account for this anomaly, is not unusual with paste bonds, Reference [5]. Factors that can contribute to bond strength scatter include surface preparation and adhesive thickness, which can vary from specimen to specimen and from side to side.

A Typical example of the measured versus predicted strains is shown in Figure 23 for sample 2. The plot shows the individual load/strain responses for each of the three gages on the particular leg that was loaded and a prediction for the center gage.
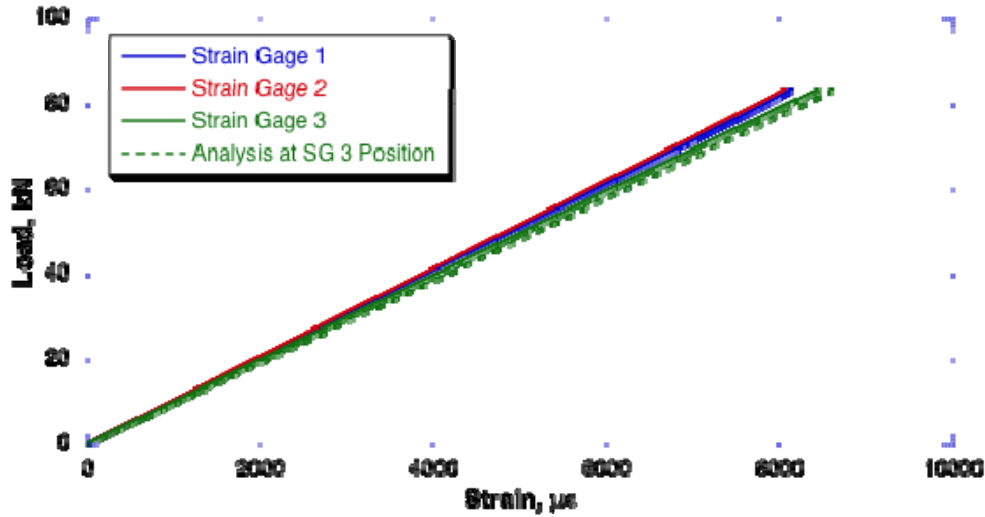

Figure 23. Sample 2 loaded in tension along the 6-10 direction

Measured and analytically obtained strains at the failure load, for all samples, are summarized in Table 8. The results indicate that the FEA model under predicted the compressive strain and consistently over predicted the tensile strains. This was consistent with the use of average (tension, compression) Young's moduli, E_1 and E_2. Overall, the analytical strains were close to the measured strains at the failure load with the greatest deviation being 5.21 %.

Table 8. Comparison of FEA and measured strains at failure load

Specimen No.	FEA Strain, µε	Measured Strain, µε	Deviation, %
1	-7,706	-7,858	-1.93
2	8,642	8,443	2.36
3a	3,556	3,442	3.31
3b	5,289	5,027	5.21
4	7,206	6,971	3.37
5b	6,333	6,236	1.55
5c	6,810	6,653	2.35

While testing of the titanium cruciform provided good modeling experience and a better understanding of the performance of the pasted joint, the titanium cruciform was not used for the full-scale backbone fabrication. Even though the design proved to be adequate for the particular application, the large strength variability of the pasted joint, as shown in Figure 22, remained somewhat of a concern. Therefore, an alternative composite joint option (woven carbon fiber pre-form cruciform), which offered a more predictable performance and fabrication option, was used instead. Development and test results of the composite cruciform are presented in Reference [2].

6. CONCLUSIONS

The scatter in the measured strength of the joints depended on the joint type (paste bond versus co-cured) and on the complexity of the joint. The co-cured main splice joint exhibited the least amount of scatter and the paste-bonded cruciform exhibited the greatest amount of scatter.

The element tests met most stated objectives and some of the tests highlighted the need for post-test non-linear analysis to capture complex deformations. For example, the asymmetry of the LIDS joint geometry and the resulting geometric non-linearity of the specimen response highlighted an inherent weakness in using linear FEA to predict the strength of such specimen. Scaling the linear-elastic FEA results to predict failure loads and modes would lead to incorrect predictions based on a false ranking of failure mode margins.

For the tapered core, test results demonstrated that exceeding the design allowable limits of the core, based on linear elastic analysis in conjunction with manufacturer supplied core properties, did not constitute catastrophic failure. Test samples failed at loads approximately equal to two times the load at which linear elastic analysis predicted the core to have reached its allowable limit. The degree to which load can be carried by the facesheets past the core design allowable, depends on several factors including loading configuration, the thickness of the facesheets, and the core taper geometry. The investigation of these effects was beyond the scope of this element test and should be the subject of a future investigation.

7. REFERENCES

[1] NESC 06-19 Composite Crew Module: Analysis Report, 2011
[2] NESC 06-019 Composite Crew Module: Materials and Processes Report, July 2011
[3] Santos. L., CCM - Splice Development Test Plan, October 2007
[4] Weng, I., CCM-LIDS Ring/Tunnel Development Test Plan, December 2007
[5] Senevirante W.P. and Tomblin J.S. ―Scatter Analysis of Composites and Adhesive Joints for Substantiation of Modern Aircraft Structures, 41st ISTC, Wichita, KA, October 19-22, 2009
[6] Blando G., Core Ramp Coupon Test Plan, ‖ December 2008.
[7] NESC 06-019 Composite Crew Module: Test Report, 2011.
[8] Schleicher E., CCM Cruciform Element Development Test Plan, October 2008.